



Tailoring the Durability of Carbon-Coated Pd Catalysts Towards Hydrogen Oxidation Reaction (HOR) in Alkaline Media

Ricardo Sgarbi¹ · Huong Doan¹ · Vincent Martin¹ · Marian Chatenet¹

Accepted: 13 November 2022 / Published online: 21 November 2022

© The Author(s), under exclusive licence to Springer Science+Business Media, LLC, part of Springer Nature 2022

Abstract

For the hydrogen oxidation reaction (HOR), platinum group metal (PGM) catalysts are still the norm, and their large initial catalytic activity is counterbalanced by their uncertain durability in alkaline environments: harsh degradations proceed, like detachment and agglomeration of metallic nanoparticles from the carbon support, as witnessed from dedicated accelerated stress tests (AST). Herein, a strategy to increase such catalysts' durability is provided, using carbon layers surrounding the Pd-based carbon-supported nanoparticles. The robustness of such catalysts, bearing 0.5- or 0.7-nm-thick carbon cap over the Pd nanoparticles, is evaluated from AST combined with several pre/post-test characterization techniques: identical location transmission electron microscopy (IL-TEM), ex situ X-ray photoelectron spectroscopy (XPS) and ex situ inductively coupled plasma mass spectrometry (ICP-MS). The carbon layer protection limits the Pd-based nanoparticles' agglomeration, detachment, and metal leaching, improving long-term catalyst durability in HOR-like operation. Thicker carbon layers surrounding the Pd nanoparticles lead to higher materials durability and lower degradation rate (larger performance stability) upon AST, compared to thinner carbon layers. In addition, the carbon-capped catalysts enable to maintain better the required Pd/PdO state of the surface that is essential for fast HOR, resulting in superior intrinsic HOR activity versus unprotected Pd/C. Overall, this work demonstrates that the activity-durability relationship can be tuned for carbon-capped catalysts.

Keywords PGM-based electrocatalyst · Carbon-coated catalyst · HOR catalysis · Identical location transmission electron microscopy

Introduction

In the past few years, the emergency need for zero CO₂ emission technologies has driven the attention of materials scientists and electrochemists to the development of alternative electrochemical systems for energy storage and conversion. In this context, electrolyzers and fuel cells are promising and complementary technologies when coupled to “clean” renewable energies [1]. Alkaline fuel cell (AFC) and anion exchange membrane fuel cell (AEMFC) have demonstrated advantages versus their acidic counterparts, as the alkaline pH renders possible to use a broader range of polymer chemistries for membrane systems, of fuels besides H₂, such as alcohols, sodium borohydride, hydrazine in liquid

environments [2–4], and the operation with low or without platinum or other platinum group metal (PGM) in the electrodes, owing to the faster kinetics of alkaline oxygen reduction reaction (ORR) [5].

Although the utilization of PGM-free catalysts has recently enabled strategic improvements in the alkaline ORR [6–8], these materials are still challenged on the hydrogen oxidation reaction (HOR) side, both for PGM-free monometallic and bimetallic electrodes [9–12]: so far, PGM-free catalysts do not achieve similar high HOR performance compared to PGM ones, at least in the beginning-of-life of the anode [9]. Nevertheless, carbon-supported PGM-based catalysts, the present standard in A(EM)FC anodes, display insufficient materials' durability, hence low stability of their performance, which challenges the long-term and large-scale deployment of alkaline fuel cells [13]. Carbon-supported PGM-based anode catalysts are relatively more degraded in alkaline than in acidic conditions [14–16], mainly following nanoparticles detachment from their support (a process driven by the PGM-catalyzed corrosion of the carbon

✉ Ricardo Sgarbi
ricardo.sgarbi-de-moraes@grenoble-inp.fr

¹ University Grenoble Alpes, University Savoie Mont Blanc, CNRS, Grenoble INP (Institute of Engineering and Management Univ. Grenoble Alpes), LEPMI, Grenoble 38000, France

support in the vicinity of the PGM nanoparticles) and, in minor extension, agglomeration [17]. The degradation of such catalysts occurs at different rates, and possibly, mechanisms, depending on the nature of the carbon substrate [18] and the ability of the PGM-based nanoparticles to oxidize CO-like species: PtRu > Pt > Pd, more active CO-like oxidation catalysts proving more unstable [19]. As such, carbon-supported Pt monometallic catalysts display higher HOR performance (as demonstrated by the hydrogen binding energy volcano plots [20]) and smaller durability in alkaline media [17, 21], compared to their Pd counterparts, that show a better balance between their pristine performance [22] and long-term durability in high pH environments [19, 23]. This, and the larger abundance of Pd versus Pt in the Earth's crust [24], led the scientific community to focus largely on Pd-based catalysts for alkaline HOR.

Different synthesis approaches of Pd-based catalysts have been studied in the literature so far, and their catalytic activity was measured in their pristine state [25, 26]; degradation studies about Pd-based materials are mainly focused on metallic nanoparticles supported on a carbon substrate (Pd/C) [16, 18, 27, 28]. Various variables have been investigated, such as modulation of the degree of graphitization of the carbon substrate [18], variations of the palladium nanoparticles size, metallic content or geometry [28], and even the nature of the electrolyte [27]. Firstly, similarly to what is reported for Pt/C [19], the direct contact between Pd nanoparticles, carbon support, and alkaline electrolyte may lead to the progressive destabilization of the nanoparticles by Pd-assisted local corrosion of the carbon substrate, producing carbonates and driving Pd nanoparticles migration, agglomeration, and/or detachment. Selecting a graphitized carbon substrate versus an amorphous one shifts the mode of Pd/C degradation from detachment and agglomeration to coalescence and dissolution/redeposition [18]; this change of degradation mechanism does however not slow down the degradation up to 1000 cycles of accelerated stress test (AST) in the diluted alkaline electrolyte (0.1–1.23 V vs. RHE in 0.1 M NaOH, 25 °C). Secondly, unsupported cubic palladium nanoparticles are more susceptible to local Ostwald ripening and associated restructuring; they lose their cubic definition after only 150 cycles of AST (0.1–0.9 V vs. RHE in 0.1 M NaOH, 25 °C) [28]. Thirdly, when the electrolyte has reducing properties (NaBH₄, hydrazine, borane, and hydrogen instead of supporting NaOH), the Pd/C instability is magnified, because the chemical reducer enables to better reduce palladium oxides at a given low vertex potential, thereby enhancing the Pd-assisted carbon corrosion upon alternation of low/high potential values [27], hence increasing the Pd nanoparticles detachment into the electrolyte [29]. Thus, if one wants to use carbon-supported Pd-based catalysts at the anode of an A(EM)FC, it is very desirable to “protect” the Pd nanoparticles, so to minimize

their deleterious effect on carbon support corrosion and, consequently, their detachment from the carbon support, in an objective to enhance their long-term catalytic activity.

As an approach to enhance the catalytic activity towards a specific reaction and/or materials durability, different types of protection on metallic/oxides nanoparticles have already been evaluated in the literature [25, 30, 31]. Herein, a strategy to synthesize amorphous carbon layers (carbon coating) surrounding palladium nanoparticles (carbon-coated Pd nanoparticles) that are themselves supported on a carbon black substrate is proposed, so to enhance the durability of HOR catalysts in alkaline media. To that goal, a one-pot synthesis is applied to tailor the carbon coating thickness, which can be varied by adapting the carbon chain length of the metal complex: carbon caps of 0.5 nm and 0.7 nm are generated from palladium (II) acetate and acetylacetonate to Pd_{acc}/C and Pd_{acc}/C catalysts, respectively. The synthesis produces directly metallic palladium nanoparticles with controlled sizes and metal content on the chosen carbon substrate (Vulcan XC72).

In this work, we perform a study involving different thicknesses of the carbon-coated Pd nanoparticles, and, for the first time, track systemically their physicochemical and electrocatalytic properties along an accelerated stress tests that mimics start/stop operation of an A(EM)FC anode ($0.1 \leq E \leq 1.23$ V vs. RHE). The AST is performed up to 1000 cycles to evaluate the long-term durability of the carbon-coated Pd/C catalysts versus their commercial Pd/C counterparts, identical location transmission electron microscopy (IL-TEM) imaging being done to monitor the morphological changes of the materials (in comparison to previous works [27, 30]). These techniques demonstrate the advantageous properties of the carbon-coated Pd/C catalysts, as well as their superior HOR performance. To understand the positive effect of the carbon coating protection and evaluate the influence of its thicknesses, ex situ techniques have been employed in complement (X-ray photoelectron spectroscopy, XPS, and inductively coupled plasma mass spectrometry, ICP-MS).

Materials and Methods

Electrocatalysts, Inks, and Thin-Layer Electrodes

Carbon-coated palladium catalysts were synthesized from the mixture of palladium (II) acetylacetonate (Sigma-Aldrich) or palladium (II) acetate (Sigma-Aldrich) with Vulcan XC72 carbon (Cabot) in the metallic proportion of 10 wt.%, following the procedure described by Gao et al. [32]. Then, the dry powder containing palladium precursor and carbon black was pyrolyzed under a neutral atmosphere (Ar) at a ramp of 45 °C min⁻¹ from room temperature to

450 °C and held at 450 °C for 30 min; depending on the palladium precursor complex, this pyrolysis produced two catalysts labeled as Pd_{acc}/C and Pd_{acc}/C, respectively. Pd/C (Premetek; 10 wt.%) was selected as the unprotected (without carbon layer surrounding the metallic nanoparticles) benchmark catalyst for further comparisons.

Catalytic inks were prepared from a mixture of desired catalytic powder (ca. 7 mg), ultrapure water (2 mL; Millipore, 18.2 MΩ cm, 1–3 ppb TOC), isopropanol (3 mL; Sigma-Aldrich), and 5 wt.% Nafion (40 μL; Sigma-Aldrich) followed by homogenization in a sonication bath (room temperature). Then, a desired amount of the ink was dropped onto a glassy carbon (0.196 cm²) tip to obtain 10 μg_{Pd} cm⁻² for rotating disk electrode (RDE) measurements. Glassy carbon plates and larger Pd loadings were employed for samples that undergone analyzes by the ex situ techniques: ICP-MS (75 μg_{Pd}) and XPS (150 μg_{Pd}), the larger Pd loadings being adapted to the detection limits of these techniques.

Electrochemical Measurements

Glassware, electrodes, plastic accessories, and PTFE-based materials were previously cleaned in Caro's acid solution (50% v/v H₂SO₄/H₂O₂) and rinsed by ultrapure water before the electrochemical procedures. All glassy carbon electrodes were mirror-polished with diamond paste (6, 3, and 1 μm) prior to their use.

Electrochemical experiments were performed in a de-aerated (under Ar or H₂ flow) 0.1 M KOH aqueous solution prepared from KOH (Alfa Aesar) pellets and ultrapure water at controlled temperature ($T=25$ °C). The three-electrode PTFE-based electrochemical cell was composed of one commercial reversible hydrogen electrode (RHE, Hydroflex), a glassy carbon sheet as the counter electrode, and a rotating disk electrode connected to the rotation speed control (or simply a glassy carbon sheet) as working (thin layer) electrode. An H-type electrochemical cell baring a glass frit separating the working electrode and the counter one was employed to avoid further metal redeposition on the counter, then quantifying more accurately the leached palladium in the electrolyte by ex situ ICP-MS. The electrochemical system was connected to a Bio-Logic potentiostat (VMP3) and monitored using the *EC-Lab* software.

Electrochemical characterization followed a sequential procedure involving cyclic voltammetry (CV) between 0.05 and 1.05 V vs. RHE for the break-in of the thin-layer electrode: (i) twenty CVs at $v=100$ mV s⁻¹ and (ii) three CVs at $v=20$ mV s⁻¹, with the second cycle (that overlaps with the third one) used to compare the electrocatalysts in terms of characteristic features of hydrogen underpotential deposition/oxidation and Pd-oxides formation/reduction. ECSA (electrochemical surface area) was calculated by integrating the PdO_x reduction peak of the first monolayer

(with the charge associated being 424 μC cm_{Pd}⁻²), in which PdO_x monolayers were previously produced at high potential during the CVs between 0.05 and 1.5 V vs. RHE at $v=20$ mV s⁻¹ [33]. The degradation procedure (accelerated stress test (AST)) consisted of potential stepping between 0.1 and 1.23 V vs. RHE with a pulse of 3 s at each potential (1 cycle = 6 s) in Ar-saturated electrolyte ($T=25$ °C). Before and post-AST, the HOR catalyst activity was quantified by slow-scan CVs between 0 and 0.5 V at $v=5$ mV s⁻¹ with RDE speed rotation of 1600 rpm in H₂-saturated electrolytes. The HOR activity of the three different catalysts was compared using three relevant kinetic markers: the mass-normalized kinetic current ($i_{k,m}^{10\text{ mV}}$; mass activity) calculated by the Koutecky-Levich equation at $E=10$ mV vs. RHE, as well as mass- ($i_{0,m}$) and surface area- ($i_{0,s}$) normalized exchange current were obtained from Tafel plot fitted by Butler-Volmer equation. All electrochemical measurements were corrected at 85% from the ohmic drop determined at open circuit potential (E_{OCP}).

X-ray Diffraction (XRD)

An X'Pert PRO MPD PANalytical diffractometer was employed to analyze the crystalline structure of catalytic powder samples. The diffractometer was operated at 45 kV and 40 mA using Cu-Kα x-ray radiation ($\lambda=1.5419$ Å) in Bragg–Brentano mode. The 2θ angle was scanned from 5° to 100° using a sweep rate of 0.1° min⁻¹. The XRD patterns were assigned using the software *Diffrac.Eva*.

Inductively Coupled Plasma Mass Spectrometry (ICP-MS)

The palladium content of the Pd_{acc}/C and Pd_{acc}/C catalysts and the (possible) palladium leaching in the electrolyte post-AST were quantified using a PerkinElmer NexION 2000 ICP-MS instrument. In the former case, the powder samples were digested in *aqua regia* (solution 1:3 HNO₃/HCl) assisted by microwave irradiation ($t=1$ h and $T=250$ °C) for complete carbon degradation and metal solubilization. In the latter case, the palladium leaching content was quantified directly into the post-AST alkaline electrolyte and estimated by the equation: $([\text{final Pd content/ppb}]_{\text{electrolyte}}/[\text{maximum Pd content/ppb}]_{\text{electrolyte}}) \times 100\%$. The determined Pd content in the initial 0.1 M KOH electrolyte was 0 ppb and the [maximum Pd content] was estimated from the total dissolution of Pd on the catalytic layer divided by the final electrolyte volume. The palladium calibration curve was made from single-element ICP-MS standard solutions (Carl Roth GmbH & Co. Kg, Germany) prepared in 0.05 mol L⁻¹ KOH with analytical solutions containing 0, 2, 5, 10, 20, and 50 ppb of palladium and 2.5 ppb ¹⁰³Rh internal standard solution (PerkinElmer). Polyatomic interference was attenuated by

Helium collision mode with kinetic energy discrimination (KED) to detect ^{108}Pd in the samples.

Transmission Electron Microscopy (TEM) and Identical Location Transmission Electron Microscopy (IL-TEM)

TEM and IL-TEM analyses were performed using a JEOL 2010 TEM instrument operated at 200 kV (LaB6 filament) with a point-to-point resolution of 0.19 nm. The samples comprised the initial and potential-cycled catalysts deposited from an ink (above described) on an Au-Lacey-carbon grid. The electrochemical (IL-TEM) measurements have consisted of the AST cycle procedures using such prepared TEM grids as the working electrode, without any previous stabilization due to the low catalyst content on the grid. The images were visualized and recorded using *Gatan Microscopy Suite* software pre- and post-AST on identical regions of the TEM grid, as detailed for example in refs. [21, 27, 34]; the Pd nanoparticle sizes and carbon coating thicknesses were determined by analyzing the micrographs using the *ImageJ* software.

X-ray Photoelectron Spectroscopy (XPS)

A Thermo Scientific K α spectrometer with a monochromated Al X-ray source ($h\nu = 1486.6$ eV; spot size 400 μm) was used to obtain the XPS patterns directly from the catalytic layers deposited onto specifically designed glassy carbon plates. The Pd 3d XPS pattern was fitted using Shirley background subtraction and LA(1.9,7,2) line shape to determine the Pd and PdO near-surface content. Binding energies were corrected by referencing the C–C component of the C 1s (sp^2 and sp^3 -hybridized carbon atoms) peak at 284.3 eV.

Results and Discussion

Catalysts Physicochemical Characterization

High-magnification TEM images of the carbon-coated Pd/C samples (Figs. 1A–B and S1), obtained from three different regions, show Pd nanoparticles wrapped by an external amorphous carbon layer (no clear graphitic planes could be detected), labeled here as the carbon coating or carbon cap. The final materials are designated as carbon-coated palladium catalysts: Pd_{ace}/C and Pd_{acc}/C. The thickness of this amorphous carbon layer was deliberately chosen to be the main physical difference between Pd_{ace}/C and Pd_{acc}/C, where Pd_{ace}/C has a thinner coating of 0.5 ± 0.05 nm surrounding Pd nanoparticles and Pd_{acc}/C has the thicker one with 0.7 ± 0.05 nm, as detected in the

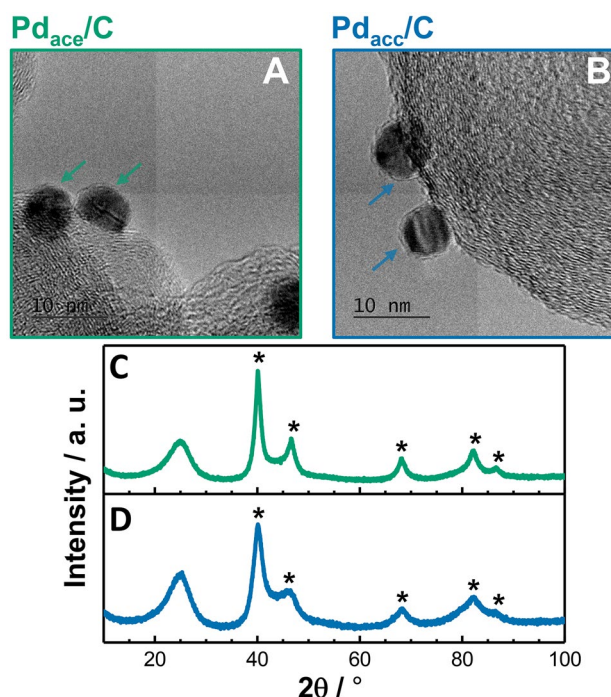


Fig. 1 High-magnification TEM images of **A** Pd_{ace}/C and **B** Pd_{acc}/C with arrows highlighting the carbon layers surrounding Pd nanoparticles. XRD patterns of **C** Pd_{ace}/C and **D** Pd_{acc}/C with assigned (*) crystalline cubic phase of metallic palladium

representative TEM micrographs and cap thickness distributions histograms of Fig. S2A and B, respectively. Varying the length of the carbon chain of the palladium precursor complexes leads to these tailored thicknesses: acetylacetonate (C₁₀) has a longer alkyl chain than acetate (C₄), producing Pd_{acc}/C and Pd_{ace}/C, respectively. According to three different TEM micrographs (Figs. 1A–B and S1–S2), the coating thickness differences do not affect the Pd nanoparticle morphology and size: their shape remains spherical, with a near-constant diameter of 6 ± 1.9 nm and 7 ± 1.6 nm for Pd_{ace}/C (Figs. S3–S4) and Pd_{acc}/C (Figs. S5–S7) materials, respectively. Commercial Pd/C catalyst also presents spherical-shaped nanoparticles, with a size of 4 ± 0.7 nm (Fig. S8), the same as found in previous work (ca. 4 nm [27]). Similarly, the Pd content is controlled by the one-pot synthesis procedure, as detected by ICP-MS analysis: the palladium-to-carbon mass is 5 wt.% (Pd_{ace}/C) and 7 wt.% (Pd_{acc}/C). In addition, based on the XRD pattern in Fig. 1C–D, only Pd metallic phase was detected by XRD in the case of the two carbon-coated catalysts (no Pd-oxide phase is detected). The metallic phase is a cubic crystalline structure of palladium (PDF 04–001–0111) with diffraction peaks set at $2\theta = 40, 47, 68, 82,$ and 87° , while both Pd and PdO phases are found on the commercial 10 wt.% Pd/C catalyst (Fig. S9). This demonstrates that the

Table 1 Physicochemical properties of the Pd_{acc}/C, Pd_{ace}/C, and Pd/C catalysts

Catalyst	Pd content/wt. %	Nanoparticle size ^a /nm	Carbon coating thickness ^a /nm	Pd crystalline phase
Pd/C	10	4 ± 0.7	-	Pd and PdO
Pd _{acc} /C	5	6 ± 1.9	0.5 ± 0.05	Pd
Pd _{ace} /C	7	7 ± 1.6	0.7 ± 0.05	Pd

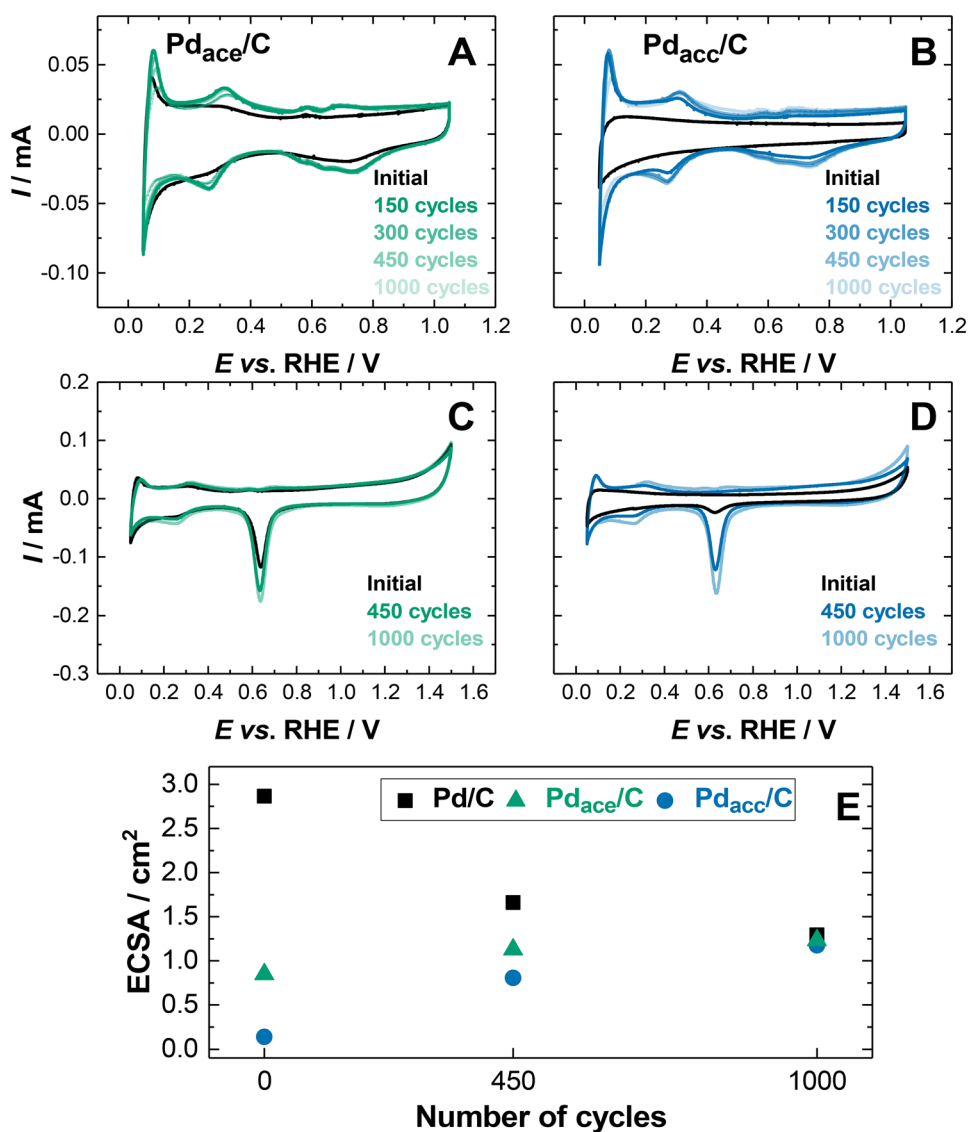
^aBased on three different TEM images

present one-pot synthesis produces protected metallic nanoparticles that resist passivation when stored in ambient conditions, unlike the commercial (unprotected) Pd/C sample. Table 1 summarizes the obtained carbon coating thickness, nanoparticles size, and metallic content of the Pd_{acc}/C, Pd_{ace}/C, and Pd/C materials.

Electrochemical Performance and Nanoparticle Morphology

To examine the catalyst materials' durability/stability in electrochemical conditions, which means mimicking the operation in an A(EM)FC system, the carbon-coated materials went through accelerated stress tests from $E=0.1$ to 1.23 V vs. RHE. This potential interval mimics the one experienced by the anode catalyst upon repeated starts (low potential, here $E=0.1$ vs. RHE) and stops (high potential, here $E=1.23$ V vs. RHE). Figures 2A–B and S10. A show the evolution of the carbon-coated and the commercial catalysts from the pristine state, post-150 cycles and up to 1000 cycles of AST. The main CV features are (i) the hydrogen adsorption/desorption on negative- and positive-going scans ($0.1 \leq E \leq 0.4$ V vs. RHE), respectively [33], (ii) adsorbed palladium oxygenated species (i.e., PdO, Pd(OH)₂); labeled

Fig. 2 Cyclic voltammetry of initial and post-AST cycles for **A–C** Pd_{ace}/C and **B–D** Pd_{acc}/C catalysts; **E** estimated ECSA along the AST cycles



here as PdO_x) formation close to $E = 0.6$ and 0.7 V vs. RHE, and (iii) PdO_x monolayer at higher potentials ($E \geq 1.4$ V vs. RHE) and the corresponding PdO_x reduction peak at $E \approx 0.7$ V vs. RHE [33]. In the pristine state (initial; black line), the CV features are significantly different for the two carbon-coated catalysts: while the Pd_{acc}/C has the typical features of palladium cyclic voltammogram (Fig. 2A), with lower currents than the commercial one (Fig. S10A), the Pd_{acc}/C has meager contributions of hydrogen and oxide-hydroxide adsorption/desorption regions (Fig. 2B). Moreover, for both carbon-coated Pd catalysts, the monolayer PdO_x reduction peaks have smaller integrated areas (Fig. 2C–D) than on the unprotected Pd/C (Fig. S10B), which further confirms that metallic nanoparticles of protected Pd are less exposed to the electrolyte, even at such high oxidation potential (1.5 V vs. RHE). The carbon coating is an amorphous (see TEM micrographs of Figs. 1A–B and S1), hence porous, barrier that might initially constrain the electrolyte access, depending on its thickness: Pd_{acc}/C has less access to the electrolyte than Pd_{acc}/C. This means that the initial electrolyte access to the palladium nanoparticles is hindered for thicker carbon coatings (Pd_{acc}/C < Pd_{acc}/C < Pd/C). To prove the above hypothesis and to understand what action is needed to “open up” the porous carbon layers so that the electrolyte, and in particular the reactant of the HOR (H₂O and OH[−]), can pass through to reach the Pd surface, standard AST condition was used; the results are presented in Fig. 2. As expected, the AST, by favoring repeated mild oxidation/reduction cycles, caused the opening of the carbon layers (led to opening and/or creation of porosities) and enhanced hydrogen and oxide-hydroxide adsorption/desorption regions post-150 cycles, as well as the monolayer PdO_x reduction peak area obtained in Fig. 2C–D after 450 and 1000 cycles of AST. Clearly, such potential cycles make the palladium nanoparticles more accessible to the electrolyte, i.e., activation process, leading the carbon-coated catalysts to have higher ECSA values in the course of the AST, as shown in Fig. 2E.

Despite the different coating thicknesses, the final ECSA reaches roughly similar values post-1000 cycles for the two protected catalysts, meaning that the Pd_{acc}/C is activating 2.5 times faster (in terms of ECSA gain: $+1.0 \times 10^{-3}$ cm² cycle^{−1}) than Pd_{acc}/C ($+0.4 \times 10^{-3}$ cm² cycle^{−1}), a similar trend being found in the first 450 cycles. In contrast, the unprotected (Pd/C) catalyst continuously and monotonously loses its ECSA, at an initial rate of -2.7×10^{-3} cm² cycle^{−1} (from 1 to 450 cycles) and then of -1.6×10^{-3} cm² cycle^{−1} (from 450 to 1000 cycles), reaching a final ECSA close to that previously reported in the literature for such AST program (Refs [18, 23, 27]). The ECSA loss for unprotected Pd/C is caused mainly by severe Pd nanoparticles detachment from the carbon support, with agglomeration as a minor contribution [18, 19, 23, 27]; in addition, the potential of the PdO_x reduction peak shifts to higher values

in Fig. S10B, a sign of Pd nanoparticles size growth following minor Ostwald ripening. These degradation processes do not occur and/or contribute to a minimal extent on both carbon-coated Pd catalysts: the coating efficiently protects the Pd nanoparticles, this protection remaining until 1000 cycles of AST. High-magnification TEM micrographs (Figs. S11–S12) show the essentially unchanged thickness of the carbon layers surrounding Pd nanoparticles post-300 and 1000 cycles (except in some regions for Pd_{acc}/C post-1000 cycles as discussed below). The thicknesses value could not be tracked statistically on high-magnification TEM mode due to the degradation of the palladium nanoparticles by the electron beam after ASTs, as exemplified by Fig. S12C–D. IL-TEM images (Fig. 3) with the respective histograms (Fig. S7) confirm the excellent stability of most carbon-coated palladium nanoparticles: agglomeration is near-avoided, and the size of the nanoparticles remains identical to the initial ones; based at least on two different regions (Figs. S3–S7), they are ca. 6 nm and ca. 7 nm even post-300 and 1000 cycles for Pd_{acc}/C and Pd_{acc}/C, respectively (summarized in Table S1).

The Role of Carbon Coating Thickness and HOR Electrocatalyst Durability

The surface chemical composition of Pd-based catalysts was evaluated by ex situ XPS; more precisely, the initial metallic content was compared to that after 450 and 1000 potential cycles of AST (details in Materials and Methods). The spectra were fitted in the Pd 3d region with two components for Pd ($3d_{5/2} = 335.1 \pm 0.1$ eV and $3d_{3/2} = 340.3 \pm 0.2$ eV) and PdO ($3d_{5/2} = 335.9 \pm 0.3$ eV and $3d_{3/2} = 341.9 \pm 0.5$ eV) [35], as shown in Fig. S13. Figure 4A and B quantify Pd and PdO species determined from fitted XPS spectra for the pristine materials: the unprotected catalyst (Pd/C Premetek) has the lowest Pd metallic content (ca. 65 at.%); similar palladium metallic contributions were also detected on other samples, such as Pd/C [36] and Pd/C TKK [37]. It is followed by Pd_{acc}/C (ca. 85 at.%) and the fully Pd metallic Pd_{acc}/C catalyst, evidencing that the thicker carbon-coated nanoparticles exhibit more metallic Pd content, which confirms the electrochemical measurements presented above (Table S2), whereas Pd nanoparticles protected by CeO_x layers with thicknesses from ca. 0.7 nm (\approx Pd_{acc}/C) to 1.3 nm show the presence of some oxidized Pd species [38].

Subsequently, a steady growing PdO tendency can be witnessed along 450 and 1000 potential cycles for Pd_{acc}/C; a similar behavior is found for Pd_{acc}/C until 450 cycles. Indeed, the AST potential window enables the palladium metallic species oxidation into PdO ($E = 0.9$ V vs. RHE); PdO/PdO₂ oxidation also may be considered since its potential ($E = 1.28$ V vs. RHE) [39] is very close to the maximum potential applied in the AST procedure ($E = 1.23$ V vs.

Fig. 3 IL-TEM images of initial and post 300 and 1000 cycles for **A–C** Pd_{ace}/C and **D–F** Pd_{acc}/C catalysts

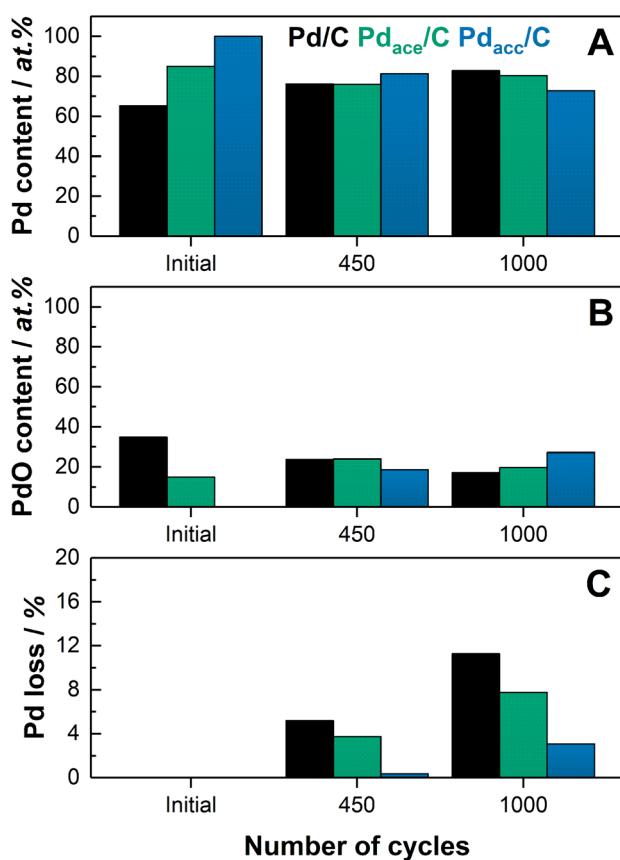
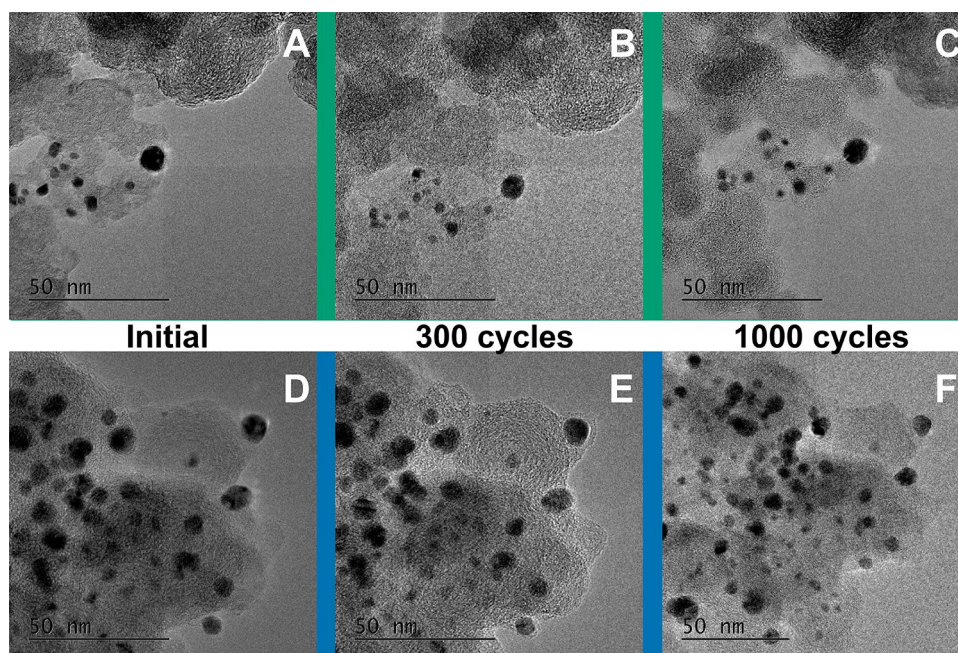


Fig. 4 XPS quantification of **A** Pd metallic and **B** PdO species on the surface of the catalyst layer, and **C** estimated Pd loss detected by ex situ ICP-MS in the bulk electrolyte for Pd/C, Pd_{ace}/C, and Pd_{acc}/C catalysts

RHE). However, the unprotected palladium nanoparticles (Pd/C) catalyst exhibits an inverse decreasing trend, with depreciation of PdO content on the near-surface, indicating the strong dissolution (see hereafter) of oxidized species into the alkaline electrolyte, in agreement with the trend monitored by IL-TEM in the previous contributions of Zadick et al. [27]. It also can be monitored by a continuous decrease of the Pd/PdO ratio, which has the “proper value” (for high HOR activity, see hereafter) for the activated and balanced catalysts, such as Pd_{ace}/C up to 450 cycles and Pd_{acc}/C (Table S2).

Palladium dissolution was quantified using ex situ ICP-MS to measure the overall Pd content in the 0.1 M KOH supporting electrolyte post-450 and 1000 cycles (details in Materials and Methods). Figure 4C shows the estimated palladium losses in the electrolyte as compared with a theoretical complete catalytic layer dissolution in the final electrolyte volume; the possible deviation from the complete layer wettability, related to the hydrophobicity feature, was disregarded. As expected, according to the previous results, the highest Pd loss is found for Pd/C (ca. 5%) followed by the thinner (Pd_{ace}/C; ca. 4%) and the thicker (Pd_{acc}/C; 0.4%) carbon-coated catalyst post-450 cycles, and ca. 12, 8, and 4% post-1000 cycles, respectively. These ICP-MS results evidence the non-negligible palladium nanoparticles dissolution along the AST cycles, especially for the unprotected Pd/C catalyst; this feature keeps up with PdO near-surface formation for Pd_{ace}/C and Pd_{acc}/C catalysts detected by XPS measurements. The detection of soluble Pd species by ICP-MS essentially scale with the Pd/PdO surface oxidation of

the catalysts, being initially high for the unprotected Pt/C, and progressively growing for the two protected Pd/C material; the electrochemical transition between these surface oxides and Pd metal during repeated potential cycling [39] indeed leads to the (transient) leaching of Pd ionic species [29]. In particular, this cathodic instability decreases the PdO content on the surface of the (unprotected) commercial catalyst, while the protective carbon coating enables most PdO species to remain stable onto the catalytic layer for Pd_{acc}/C and Pd_{acc}/C, for at least up to 450 cycles. A thicker carbon layer (Pd_{acc}/C) protects more the palladium nanoparticles from dissolution throughout the investigated potential cycles than thinner ones (Pd_{acc}/C) and slows down their degradation. Similarly, Speck et al. [38] have demonstrated a clear decline tendency of Pd dissolution with the rising of CeO_x layer thickness in H₂-saturated 0.05 M NaOH electrolyte.

However, effective protection is not unlimited; it reaches a maximum between 450 and 1000 cycles for the thinner coating (Pd_{acc}/C): the PdO content grows up to 450 cycles, while for Pd_{acc}/C (thicker one) the growth occurs until 1000 cycles. In opposition, the unprotected Pd/C continuously loses its PdO content over the AST. Thus, according to the number of AST cycles, the Pd_{acc}/C catalyst follows an intermediate behavior between the thickest carbon-coated catalyst and the unprotected one. This means that the degree of protection or the activation energy can be tailored by the thickness of the carbon layer.

In order to evaluate the HOR performance of the protected vs. unprotected catalysts, HOR polarization curves were measured at pristine state and post 150, 300, 450, and 1000 cycles of AST, following the degradation procedure detailed above. The HOR characteristics are shown in Fig. 5A–C for commercial, Pd/C, Pd_{acc}/C, and Pd_{acc}/C catalysts, respectively. In the pristine state, Pd_{acc}/C has a high current in the kinetic region ($E \approx 10$ mV vs. RHE) and a well-defined diffusion-convection region ($0.3 \leq E \leq 0.5$ V vs. RHE), the latter being near-similar to that monitored for Pd/C and in literature [22]. The Pd_{acc}/C catalyst exhibits a typical HOR polarization curve of a low-active catalyst in either the kinetic and diffusion-convection-limited regions: the thickest coating catalyst requires an extra activation by 150 cycles, only reaching similar current density magnitudes as for the pristine Pd_{acc}/C and Pd/C after this prolonged activation; it confirms that the contact between the electrolyte and the more-or-less protected palladium nanoparticles can be improved by proper “activation” of the material. The optimal HOR activity seems to require a proper interplay between Pd and PdO surface sites [12, 31, 36, 40, 41], which are initially present on Pd_{acc}/C and Pd/C, but not on Pd_{acc}/C.

Less protected and unprotected, Pd_{acc}/C and Pd/C, respectively, nanoparticles experience a non-negligible degradation of their HOR performance post-150 cycles, with similar

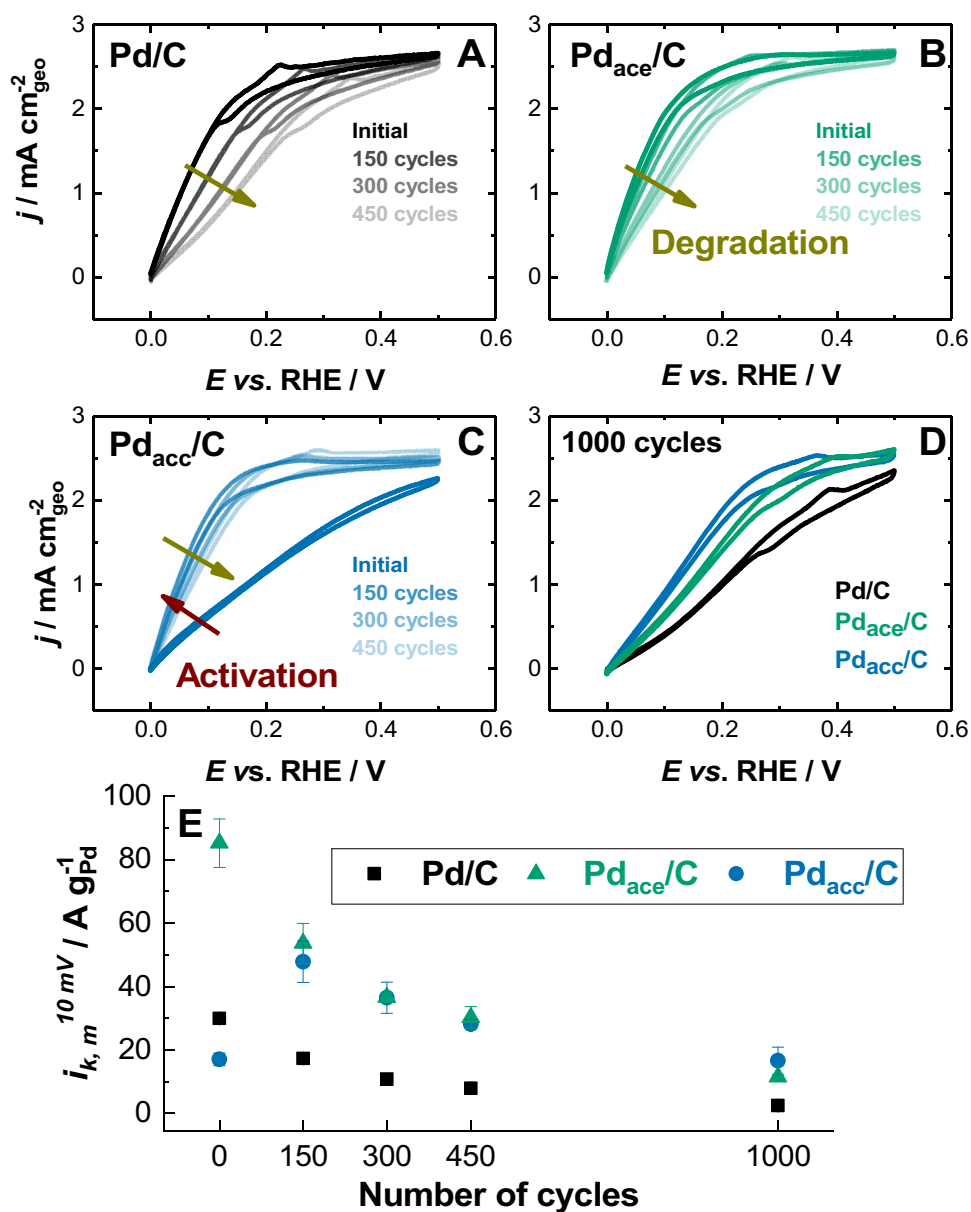
descending features up to 1000 cycles; the “more protected” Pd_{acc}/C sample witnesses a less-degraded HOR behavior in the course of the AST, evidenced in Fig. 5D.

Figure 5E presents the mass-normalized kinetic current at 10 mV vs. RHE ($i_{k,m}^{10\text{mV}}$), both for the initial and post-AST states of the catalysts: the highest initial HOR mass activity is monitored for Pd_{acc}/C (85.2 ± 7.6 A g_{Pd}⁻¹); together with the activated-Pd_{acc}/C (> 150 cycles; 47.8 ± 6.5 A g_{Pd}⁻¹), they have ca. 3- and twofold higher HOR mass activity than commercial Pd/C, respectively, which can again be associated with a maintained optimal Pd/PdO coverage at the catalyst particles surface in the course of the AST, whereas the PdO species are irremediably leached for unprotected Pd/C. Likewise, the surface-normalized exchange currents ($i_{0,s}$), obtained by fitting the Tafel plot (Fig. S14), are 3- to fourfold higher for Pd_{acc}/C (> 150 cycles; 88.1 ± 1.0 μA cm⁻²_{Pd}) and Pd_{acc}/C (75.5 ± 3.9 μA cm⁻²_{Pd}) than the commercial one (Table S3). It indicates that the carbon coating thickness influences the magnitude of the kinetic parameters: while the external carbon protection likely enables to maintain the metal nanoparticle in its optimal Pd/PdO configuration for fast HOR, as similarly reported in the literature for PGM and PGM-free encapsulated electrocatalysts and/or heteroatoms-doped carbon substrates [42–46], thick carbon layers slow down the initial activation process (formation of PdO from initially metallic Pd nanoparticles) of carbon-coated Pd nanoparticles

The carbon-coated catalysts HOR mass activities, based on $i_{k,m}^{10\text{mV}}$, are kept between 3- and sevenfold better than for the commercial Pd/C benchmark along the investigated number of cycles, as represented in Fig. 5E. After 1000 cycles of AST, the two carbon-capped Pd/C catalysts still retain at least the initial HOR activity measured on unprotected Pd/C, which itself has an activity degraded by ca. sixfold compared to this value. Similar trends are measured for $i_{0,m}$ and $i_{0,s}$, which means that the high and maintained HOR activity of the carbon-coated catalysts is a result of a combination of their maintained Pd/PdO surface ratio and of their reduced morphological degradations (reduced Pd detachment, leaching, and minimum (or absence) nanoparticles agglomeration) upon AST compared to the commercial Pd/C sample. However, the degradation rate of HOR performance is more pronounced for the thinnest coating catalyst (from 211 to 74 mA g_{Pd}⁻¹ cycle⁻¹) than the thickest (from 75 to 37 mA g_{Pd}⁻¹ cycle⁻¹) and unprotected one (from 84 to 28 mA g_{Pd}⁻¹ cycle⁻¹). As the coating thickness grows from 0.5 nm to 0.7 nm, a *circa* twofold slower degradation rate is monitored in favor of the thicker catalyst (Pd_{acc}/C), the materials still displaying significantly higher HOR performance than Pd/C catalyst from 150 to 1000 cycles.

Despite the slow rate of Pd leaching for Pd_{acc}/C and Pd_{acc}/C, the HOR mass activity still decreases along the potential cycling procedure from 0 and 150 cycles to 1000

Fig. 5 HOR polarization curves for initial and post-AST cycles for **A** commercial Pd/C, **B** Pd_{ace}/C, **C** Pd_{acc}/C catalysts, and **D** comparison post-1000 cycles; **E** mass-normalized kinetic current at $E = 10$ mV vs. RHE ($i_{k,m}^{10\text{mV}}$) along AST cycles

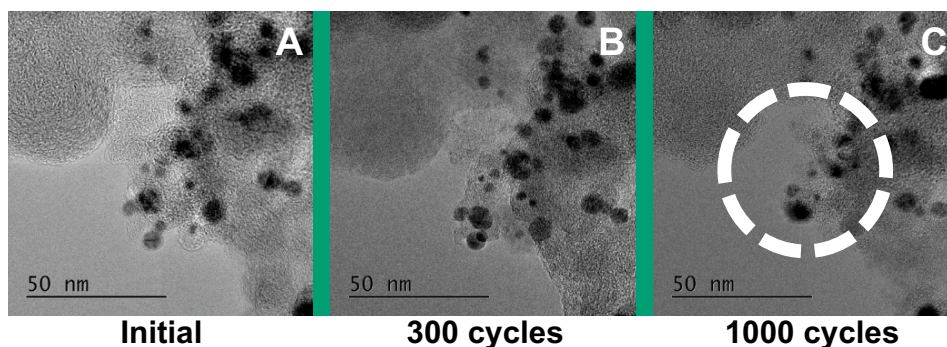


cycles, respectively. It may be attributed to two main contributions: (i) some nanoparticles detachment caused by the Pd-catalyzed oxidation of the carbonaceous matrix, as proposed by Lafforgue et al. [19] is possible and is visualized here by IL-TEM images (Fig. 6) in minor regions (white circles) of the thinnest carbon-coated catalyst post-1000 cycles. Those nanoparticle losses occur in a much lower extent than for the commercial Pd/C sample, as demonstrated by the recorded electrochemical features, ex situ ICP-MS and in refs. [27, 30]. However, combined with a small extent of Ostwald ripening and nanoparticles growth (also seen in Fig. 6 and larger range distribution in Table S2), it seems enough to drop the nanoparticle density in a few (but detectable by IL-TEM) regions for Pd_{acc} catalyst. A second contribution is (ii) the partial interconversion of metallic Pd to

oxides species (ca. 20–27%); too extensive PdO formation depreciates the HOR activity since carbon-supported PdO has lower HOR mass activity than Pd in the same conditions [47] and since the Pd/PdO surface ratio needs to be optimal for fast HOR [31, 36, 40, 41]. In addition, an intrinsic small electrical conductivity of oxides versus metallic particles could add to this depreciated HOR activity versus AST cycling.

A durability enhancement using the thickest (ca. 0.7 nm) carbon coating on Pd catalysts makes this type of catalyst really advantageous versus an unprotected one for prolonged HOR operation in alkaline conditions. However, the intrinsic feature of PGMs to catalyze the carbon oxidation reaction, even being less catalyzed for Pd than Pt and PtRu [19], still requires improvements in their chemical composition.

Fig. 6 IL-TEM images evidencing the degraded region post-1000 cycles (white circle) for A–C Pd_{acc}/C catalyst



This statement and the current experimental results suggest that bimetallic carbon-coated catalysts may consist of a better combination of activity and durability, owing to the improved catalytic performance of bimetallic/bifunctional materials [48–50] and better durability of Pd-M alloys versus monometallic towards HOR catalysis [51]. This is the next step that will soon be evaluated by the team.

Conclusions

A one-pot method employed in this work enables to synthesize well-controlled carbon-coated palladium nanoparticles, in terms of the carbon layer thickness (based on the carbon chain length of metal precursor complexes), Pd nanoparticles size, and metallic content. The carbon layer surrounding palladium nanoparticles improves the HOR activity (its maximum being reached after a necessary activation step) and long-term durability of the materials versus potential cycling in alkaline conditions. This is mainly ascribed to the protection features of the carbon coating, which on the one hand limits nanoparticle agglomeration, avoids detachment, and slows down metallic leaching out to the electrolyte, while helps to maintain dual Pd/PdO surface species that enable fast HOR. These advantageous features are even more apparent on the thicker carbon-coated catalyst (Pd_{acc}/C), with a ca. 0.7-nm-thick carbon cap. The latter however requires an extra activation of 150 cycles between $0.1 \leq E \leq 1.23$ V vs. RHE compared to the thinner carbon-coated catalyst (Pd_{acc}/C; 0.5-nm-thick carbon cap) to reach its maximal HOR activity. Lower metal losses obtained for the carbon-coated materials upon AST enable the protected Pd/C catalysts to show better HOR catalysis performance than the commercial post-1000 cycles of AST, their intrinsic HOR performance being also advantageous at shorter time scales. This long-term durability towards HOR performance is even higher on Pd_{acc}/C, which exhibits the lowest degradation rate and highest HOR performance upon the electrochemical cycling. Overall, the two carbon-capped Pd/C catalysts outperform unprotected Pd/C, rendering their use in A(EM)FC anodes promising.

Supplementary Information The online version contains supplementary material available at <https://doi.org/10.1007/s12678-022-00794-8>.

Acknowledgements Some of this work has been performed within the framework of the Centre of Excellence of Multifunctional Architected Materials (CEMAM), Grenoble France n° ANR-10-LABX-44-01. The authors thank Laurent Artaud from SIMaP (Science et Ingénierie des Matériaux et Procédés) for his help in handling the tube furnace and Thierry Encinas from CMTC (Consortium des Moyens Technologiques Communs) for his support on XRD analysis. H. D. would like to thank Robert Allen for his previous guidance on the chelating metal complex synthesis.

Author Contribution Ricardo Sgarbi: data curation; drawing; formal analysis; investigation; methodology; sample collection and analysis; writing—original draft; Huong Doan: data curation; drawing; formal analysis; investigation; methodology; sample collection and analysis; Vincent Martin: data curation; formal analysis; ICP-MS measurements; Marian Chatenet: conceptualization; data curation; drawing; formal analysis; funding acquisition; methodology; project administration; resources; supervision; validation; visualization; writing—review and editing.

Funding This research has benefited from the characterization equipment of the Grenoble INP – CMTC platform supported by the Centre of Excellence of Multifunctional Architected Materials (CEMAM) n° ANR-10-LABX-44-01 funded by the “Investments for the Future” Program.

Data Availability The data supporting this paper is available within the manuscript and its supporting information.

Declarations

Ethics Approval Not applicable.

Consent to Participate Not applicable.

Consent for Publication The authors declare that they consent to the publication of this paper.

Conflict of Interest The authors declare no competing interests.

References

1. J. Brauns, T. Turek, Alkaline water electrolysis powered by renewable energy: A review, *Processes*. **8** (2020). <https://doi.org/10.3390/pr8020248>

- D.R. Dekel, Review of cell performance in anion exchange membrane fuel cells. *J. Power Sources*. **375**, 158–169 (2018). <https://doi.org/10.1016/j.jpowsour.2017.07.117>
- A. Oshchepkov, A. Bonnefont, G. Maranzana, E.R. Savinova, M. Chatenet, Direct borohydride fuel cells: A selected review of their reaction mechanisms, electrocatalysts and influence of operating parameters on their performance. *Curr. Opin. Electrochem.* 100883 (2021). <https://doi.org/10.1016/j.coelec.2021.100883>
- R. Sgarbi, E.A. Ticianelli, F. Maillard, F. Jaouen, M. Chatenet, Oxygen reduction reaction on metal and nitrogen – doped carbon electrocatalysts in the presence of sodium borohydride. *Electrocatalysis* **11**, 365–373 (2020). <https://doi.org/10.1007/s12678-020-00602-1>
- A. Serov, I.V. Zenyuk, C.G. Arges, M. Chatenet, Hot topics in alkaline exchange membrane fuel cells. *J. Power Sources*. **375**, 149–157 (2018). <https://doi.org/10.1016/j.jpowsour.2017.09.068>
- R. Sgarbi, K. Kumar, F. Jaouen, A. Zitolo, E.A. Ticianelli, F. Maillard, Oxygen reduction reaction mechanism and kinetics on M-NxCy and M@N-C active sites present in model M-N-C catalysts under alkaline and acidic conditions. *J. Solid State Electrochem.* **25**, 45–56 (2021). <https://doi.org/10.1007/s10008-019-04436-w>
- R. Sgarbi, K. Kumar, V.A. Saveleva, L. Dubau, R. Chattot, V. Martin, M. Mermoux, P. Bordet, P. Glatzel, E.A. Ticianelli, F. Jaouen, F. Maillard, Electrochemical transformation of Fe-N-C catalysts into iron oxides in alkaline medium and its impact on the oxygen reduction reaction activity. *Appl. Catal. B Environ.* **311**, 121366 (2022). <https://doi.org/10.1016/j.apcatb.2022.121366>
- P.G. Santori, F.D. Speck, S. Cherevko, H.A. Firouzjaie, X. Peng, W.E. Mustain, F. Jaouen, High performance FeNC and Mn-oxide/FeNC layers for AEMFC cathodes. *J. Electrochem. Soc.* **167**, 134505 (2020). <https://doi.org/10.1149/1945-7111/abb7e0>
- A.G. Oshchepkov, G. Braesch, A. Bonnefont, E.R. Savinova, M. Chatenet, Recent advances in the understanding of nickel-based catalysts for the oxidation of hydrogen-containing fuels in alkaline media. *ACS Catal.* **10**, 7043–7068 (2020). <https://doi.org/10.1021/acscatal.0c00101>
- M.V. Pagliaro, H.A. Miller, C. Evangelisti, M. Bellini, G. Tuci, C. Pham-Huu, G. Giambastiani, M. Marelli, F. Vizza, Synergy between nickel nanoparticles and N-enriched carbon nanotubes enhances alkaline hydrogen oxidation and evolution activity. *ACS Appl. Nano Mater.* **4**, 3586–3596 (2021). <https://doi.org/10.1021/acsnm.1c00118>
- A.G. Oshchepkov, A. Bonnefont, S.N. Pronkin, O.V. Cherstiouk, C. Ulhaq-Bouillet, V. Papaefthimiou, V.N. Parmon, E.R. Savinova, Nanostructured nickel nanoparticles supported on vulcan carbon as a highly active catalyst for the hydrogen oxidation reaction in alkaline media. *J. Power Sources*. **402**, 447–452 (2018). <https://doi.org/10.1016/j.jpowsour.2018.09.051>
- J. Biemolt, J.C. Douglin, R.K. Singh, E.S. Davydova, N. Yan, G. Rothenberg, D.R. Dekel, An anion-exchange membrane fuel cell containing only abundant and affordable materials. *Energy Technol.* **9**, 5–9 (2021). <https://doi.org/10.1002/ente.202000909>
- W.E. Mustain, M. Chatenet, M. Page, Y.S. Kim, Durability challenges of anion exchange membrane fuel cells. *Energy Environ. Sci.* **13**, 2805–2838 (2020). <https://doi.org/10.1039/d0ee01133a>
- A. Kormányos, F.D. Speck, K.J.J. Mayrhofer, S. Cherevko, Influence of fuels and pH on the dissolution stability of bifunctional PtRu/C alloy electrocatalysts. *ACS Catal.* **10**, 10858–10870 (2020). <https://doi.org/10.1021/acscatal.0c02094>
- T.J.P. Hersbach, A.C. Garcia, T. Kroll, D. Sokaras, M.T.M. Koper, A.T. Garcia-Esparza, Base-accelerated degradation of nanosized platinum electrocatalysts. *ACS Catal.* **11**, 9904–9915 (2021). <https://doi.org/10.1021/acscatal.1c02468>
- C. Lafforgue, A. Zadick, L. Dubau, F. Maillard, M. Chatenet, Selected review of the degradation of Pt and Pd-based carbon-supported electrocatalysts for alkaline fuel cells: towards mechanisms of degradation. *Fuel Cells*. **18**, 229–238 (2018). <https://doi.org/10.1002/face.201700094>
- C. Lafforgue, M. Chatenet, L. Dubau, D.R. Dekel, Accelerated stress test of Pt/C nanoparticles in an interface with an anion-exchange membrane - an identical-location transmission electron microscopy study. *ACS Catal.* **8**, 1278–1286 (2018). <https://doi.org/10.1021/acscatal.7b04055>
- S. Kabir, A. Zadick, P. Atanassov, L. Dubau, M. Chatenet, Stability of carbon-supported palladium nanoparticles in alkaline media: A case study of graphitized and more amorphous supports. *Electrochem. Commun.* **78**, 33–37 (2017). <https://doi.org/10.1016/j.elecom.2017.03.017>
- C. Lafforgue, F. Maillard, V. Martin, L. Dubau, M. Chatenet, Degradation of carbon-supported platinum-group-metal electrocatalysts in alkaline media studied by in situ Fourier transform infrared spectroscopy and identical-location transmission electron microscopy. *ACS Catal.* **9**, 5613–5622 (2019). <https://doi.org/10.1021/acscatal.9b00439>
- R. Zhao, X. Yue, Q. Li, G. Fu, J.M. Lee, S. Huang, Recent advances in electrocatalysts for alkaline hydrogen oxidation reaction. *Small*. **17** (2021). <https://doi.org/10.1002/sml.202100391>
- A. Zadick, L. Dubau, N. Sergent, G. Berthomé, M. Chatenet, Huge instability of Pt/C catalysts in alkaline medium. *ACS Catal.* **5**, 4819–4824 (2015). <https://doi.org/10.1021/acscatal.5b01037>
- J. Durst, A. Siebel, C. Simon, F. Hasché, J. Herranz, H.A. Gasteiger, New insights into the electrochemical hydrogen oxidation and evolution reaction mechanism. *Energy Environ. Sci.* **7**, 2255–2260 (2014). <https://doi.org/10.1039/c4ee00440j>
- A. Zadick, L. Dubau, M. Chatenet, U. Demirci, A. Serov, P. Atanassov, Instability of commercial Pt/C and Pd/C electrocatalysts in alkaline media. *ECS Trans.* **69**, 553–558 (2015). <https://doi.org/10.1149/06917.0553ecst>
- P.C.K. Vesborg, T.F. Jaramillo, Addressing the terawatt challenge: Scalability in the supply of chemical elements for renewable energy. *RSC Adv.* **2**, 7933–7947 (2012). <https://doi.org/10.1039/c2ra20839c>
- B. Zhang, G. Zhao, B. Zhang, L. Xia, Y. Jiang, T. Ma, M. Gao, W. Sun, H. Pan, Lattice-confined Ir clusters on Pd nanosheets with charge redistribution for the hydrogen oxidation reaction under alkaline conditions. *Adv. Mater.* **33**, 22–28 (2021). <https://doi.org/10.1002/adma.202105400>
- A.K. Ipadeola, P.V. Mwonga, K.I. Ozoemena, Hydrogen oxidation and oxygen reduction reactions on palladium nano-electrocatalyst supported on nickel-deficient MOF-derived carbons. *Electrochim. Acta*. **390**, 138860 (2021). <https://doi.org/10.1016/j.electacta.2021.138860>
- A. Zadick, L. Dubau, U.B. Demirci, M. Chatenet, Effects of Pd nanoparticle size and solution reducer strength on Pd/C electrocatalyst stability in alkaline electrolyte. *J. Electrochem. Soc.* **163**, F781–F787 (2016). <https://doi.org/10.1149/2.0141608jes>
- A. Zadick, L. Dubau, A. Zalineeva, C. Coutanceau, M. Chatenet, When cubic nanoparticles get spherical: An identical location transmission electron microscopy case study with Pd in alkaline media. *Electrochem. Commun.* **48**, 1–4 (2014). <https://doi.org/10.1016/j.elecom.2014.07.020>
- M. Schalenbach, O. Kasian, M. Ledendecker, F.D. Speck, A.M. Mingers, K.J.J. Mayrhofer, S. Cherevko, The electrochemical dissolution of noble metals in alkaline media. *Electrocatalysis* **9**, 153–161 (2018). <https://doi.org/10.1007/s12678-017-0438-y>
- H.A. Miller, F. Vizza, M. Marelli, A. Zadick, L. Dubau, M. Chatenet, S. Geiger, S. Cherevko, H. Doan, R.K. Pavlicek, S. Mukerjee, D.R. Dekel, Highly active nanostructured palladium-mercuria electrocatalysts for the hydrogen oxidation reaction in

- alkaline medium. *Nano Energy* **33**, 293–305 (2017). <https://doi.org/10.1016/j.nanoen.2017.01.051>
31. H. Doan, I. Kendrick, R. Blanchard, Q. Jia, E. Knecht, A. Freeman, T. Jankins, M.K. Bates, S. Mukerjee, Functionalized embedded mono-metallic nickel catalysts for enhanced hydrogen evolution: Performance and stability. *J. Electrochem. Soc.* **168**, 084501 (2021). <https://doi.org/10.1149/1945-7111/ac11a1>
 32. Y. Gao, H. Peng, Y. Wang, G. Wang, L. Xiao, J. Lu, L. Zhuang, Improving the antioxidation capability of the Ni catalyst by carbon shell coating for alkaline hydrogen oxidation reaction. *ACS Appl. Mater. Interfaces.* **12**, 31575–31581 (2020). <https://doi.org/10.1021/acsami.0c10784>
 33. M. Grdeń, M. Łukaszewski, G. Jerkiewicz, A. Czerwiński, Electrochemical behaviour of palladium electrode: Oxidation, electrodis-solution and ionic adsorption. *Electrochim. Acta.* **53**, 7583–7598 (2008). <https://doi.org/10.1016/j.electacta.2008.05.046>
 34. F.R. Nikkuni, E.A. Ticianelli, L. Dubau, M. Chatenet, Identical-location transmission electron microscopy study of Pt/C and Pt-Co/C nanostructured electrocatalyst aging: Effects of morphological and compositional changes on the oxygen reduction reaction activity. *Electrocatalysis* **4**, 104–116 (2013). <https://doi.org/10.1007/s12678-013-0126-5>
 35. J.R.J.R. C.D. Wagner, A.V. Naumkin, A. Kraut-Vass, J.W. Allison, C.J. Powell, NIST Standard Reference Database 20, Version 3.4 (web version). (2003). <https://srdata.nist.gov/xps/>. Accessed October 21, 2021
 36. H. Yu, E.S. Davydova, U. Ash, H.A. Miller, L. Bonville, D.R. Dekel, R. Maric, Palladium-ceria nanocatalyst for hydrogen oxidation in alkaline media: Optimization of the Pd–CeO₂ interface. *Nano Energy* **57**, 820–826 (2019). <https://doi.org/10.1016/j.nanoen.2018.12.098>
 37. X. Qin, L. Zhang, G.L. Xu, S. Zhu, Q. Wang, M. Gu, X. Zhang, C. Sun, P.B. Balbuena, K. Amine, M. Shao, The role of Ru in improving the activity of Pd toward hydrogen evolution and oxidation reactions in alkaline solutions. *ACS Catal.* **9**, 9614–9621 (2019). <https://doi.org/10.1021/acscatal.9b01744>
 38. F.D. Speck, F.S.M. Ali, M.T.Y. Paul, R.K. Singh, T. Böhm, A. Hofer, O. Kasian, S. Thiele, J. Bachmann, D.R. Dekel, T. Kallio, S. Cherevko, Improved hydrogen oxidation reaction activity and stability of buried metal-oxide electrocatalyst interfaces. *Chem. Mater.* **32**, 7716–7724 (2020). <https://doi.org/10.1021/acs.chemmater.0c02048>
 39. M. Pourbaix, Atlas of electrochemical equilibria in aqueous solutions, National Association of Corrosion Engineers, Houston. (1974)
 40. J. Zheng, W. Sheng, Z. Zhuang, B. Xu, Y. Yan, Universal dependence of hydrogen oxidation and evolution reaction activity of platinum-group metals on pH and hydrogen binding energy. *Sci. Adv.* **2**, 1–9 (2016). <https://doi.org/10.1126/sciadv.1501602>
 41. A.G. Oshchepkov, A. Bonnefont, V.N. Parmon, E.R. Savinova, On the effect of temperature and surface oxidation on the kinetics of hydrogen electrode reactions on nickel in alkaline media. *Electrochim. Acta.* **269**, 111–118 (2018). <https://doi.org/10.1016/j.electacta.2018.02.106>
 42. J. Wang, X. Dong, J. Liu, W. Li, L.T. Røling, J. Xiao, L. Jiang, Ultrafine nickel nanoparticles encapsulated in N-doped carbon promoting hydrogen oxidation reaction in alkaline media. *ACS Catal.* **11**, 7422–7428 (2021). <https://doi.org/10.1021/acscatal.1c01284>
 43. Q. Liu, M. Ranocchiari, J.A. Van Bokhoven, Catalyst overcoating engineering towards high-performance electrocatalysis. *Chem. Soc. Rev.* **51**, 188–236 (2022). <https://doi.org/10.1039/d1cs00270h>
 44. W. Ni, T. Wang, F. Héroguel, A. Krammer, S. Lee, L. Yao, A. Schüler, J.S. Luterbacher, Y. Yan, X. Hu, An efficient nickel hydrogen oxidation catalyst for hydroxide exchange membrane fuel cells. *Nat. Mater.* **21** (2022). <https://doi.org/10.1038/s41563-022-01221-5>
 45. F. Yang, X. Bao, Y. Zhao, X. Wang, G. Cheng, W. Luo, Enhanced HOR catalytic activity of PGM-free catalysts in alkaline media: The electronic effect induced by different heteroatom doped carbon supports. *J. Mater. Chem. A.* **7**, 10936–10941 (2019). <https://doi.org/10.1039/c9ta01916b>
 46. Z.-C. Yao, T. Tang, Z. Jiang, L. Wang, J.-S. Hu, L.-J. Wan, Electrocatalytic hydrogen oxidation in alkaline media: From mechanistic insights to catalyst design. *ACS Nano* (2022). <https://doi.org/10.1021/acsnano.2c00641>
 47. R. Samanta, R. Mishra, S. Barman, Interface- and surface-engineered PdO–RuO₂ hetero-nanostructures with high activity for hydrogen evolution/oxidation reactions. *Chemsuschem* **14**, 2112–2125 (2021). <https://doi.org/10.1002/cssc.202100200>
 48. H. Doan, T. Morais, N. Borchtkhoukova, Y. Wijsboom, R. Sharabi, M. Chatenet, G. Finkelshtain, Bimetallic Pt or Pd-based carbon supported nanoparticles are more stable than their monometallic counterparts for application in membraneless alkaline fuel cell anodes. *Appl. Catal. B Environ.* **301**, 120811 (2022). <https://doi.org/10.1016/j.apcatb.2021.120811>
 49. M. Alesker, I. Bakos, V. Davies, Q. Jia, L. Burlaka, V. Yarmiayev, A. Muzikansky, A. Kitayev, M. Page, S. Mukerjee, D. Zitoun, Operando X-ray absorption spectroscopy of a Pd/γ-NiOOH 2 nm cubes hydrogen oxidation catalyst in an alkaline membrane fuel cell, *Catal. Sci. Technol.* **11**, 1337–1344 (2021). <https://doi.org/10.1039/d0cy01815e>
 50. S. Sahoo, D.R. Dekel, R. Maric, S.P. Alpay, Atomistic insights into the hydrogen oxidation reaction of palladium-ceria bifunctional catalysts for anion-exchange membrane fuel cells. *ACS Catal.* **11**, 2561–2571 (2021). <https://doi.org/10.1021/acscatal.0c04646>
 51. A. Zadick, L. Dubau, K. Artyushkova, A. Serov, P. Atanassov, M. Chatenet, Nickel-based electrocatalysts for ammonia borane oxidation: Enabling materials for carbon-free-fuel direct liquid alkaline fuel cell technology. *Nano Energy* **37**, 248–259 (2017). <https://doi.org/10.1016/j.nanoen.2017.05.035>

Publisher's Note Springer Nature remains neutral with regard to jurisdictional claims in published maps and institutional affiliations.

Springer Nature or its licensor (e.g. a society or other partner) holds exclusive rights to this article under a publishing agreement with the author(s) or other rightsholder(s); author self-archiving of the accepted manuscript version of this article is solely governed by the terms of such publishing agreement and applicable law.